

Predicting Frictional Properties of Graphene Kirigami Using Molecular Dynamics and Neural Networks

Designs for a negative friction coefficient.

Mikkel Metzsch Jensen



Thesis submitted for the degree of
Master in Computational Science: Materials Science
60 credits

Department of Physics
Faculty of mathematics and natural sciences

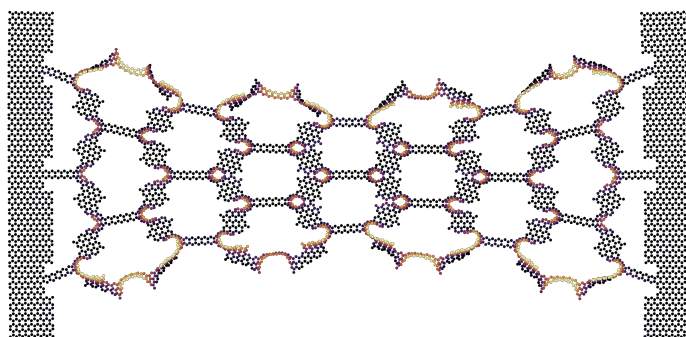
UNIVERSITY OF OSLO

Spring 2023

Predicting Frictional Properties of Graphene Kirigami Using Molecular Dynamics and Neural Networks

Designs for a negative friction coefficient.

Mikkel Metzsch Jensen



© 2023 Mikkel Metzsch Jensen

Predicting Frictional Properties of Graphene Kirigami Using Molecular Dynamics and Neural Networks

<http://www.duo.uio.no/>

Printed: Reprosentralen, University of Oslo

Abstract

Abstract.

Acknowledgments

Acknowledgments.

List of Symbols

F_N Normal force (normal load)

Acronyms

CM Center of Mass. 14, 15

MD Molecular Dynamics. 1, 2, 3, 9, 10, 13, 24

ML Machine Learning. 2, 3, 10

std Standard Deviation. 16, 17, 20, 22

Contents

1	Introduction	1
1.1	Motivation	1
1.2	Goals	2
1.3	Contributions	3
1.4	Thesis structure	3
I	Background Theory	5
II	Simulations	7
2	Pilot study	9
2.1	Friction simulation parameters	9
2.2	Force traces	10
2.2.1	Force oscillations	10
2.2.2	Decompositions	14
2.2.3	Center of mass path	14
2.3	Defining metrics for friction	16
2.3.1	Kinetic friction	16
2.3.2	Static friction	17
2.4	Out-of-plane buckling	18
2.5	Investigating main parameters	20
2.5.1	Computational cost	22
2.6	Load and stretch dependencies	23
2.6.1	Pressure reference for normal load	24
2.6.2	Stretch dependencies	24
2.6.3	Load dependency	26
	Appendices	29
	Appendix A	31
	Appendix B	33
	Appendix C	35

Chapter 1

Introduction

1.1 Motivation

Friction is the force that prevents the relative motion of objects in contact. Even though the everyday person might not be familiar with the term *friction* we recognize it as the inherent resistance to sliding motion. Some surfaces appear slippery and some rough, and we know intuitively that sliding down a snow-covered hill is much more exciting than its grassy counterpart. Without friction, it would not be possible to walk across a flat surface, lean against the wall without falling over or secure an object by the use of nails or screws [p. 5] [1]. It is probably safe to say that the concept of friction is integrated into our everyday life to such an extent that most people take it for granted. However, the efforts to control friction date back to the early civilization (3500 B.C.) with the use of the wheel and lubricants to reduce friction in translational motion [2]. Today, friction is considered a part of the wider field *tribology* derived from the Greek word *Tribos* meaning “rubbing” and includes the science of friction, wear and lubrication [2]. The most compelling motivation to study tribology is ultimately to gain full control of friction and wear for various technical applications. Especially, reducing friction is of great interest as this has tremendous advantages for energy efficiency. It has been reported that tribological problems have a significant potential for economic and environmental improvements [3]:

“On global scale, these savings would amount to 1.4% of the GDP annually and 8.7% of the total energy consumption in the long term.” [4].

On the other hand, the reduction of friction is not the only sensible application for tribological studies. Controlling frictional properties, besides minimization, might be of interest in the development of a grasping robot where finetuned object handling is required. While achieving a certain “constant” friction response is readily obtained through appropriate material choices during manufacturing, we are yet to unlock the capabilities to alter friction dynamically on the go. One example from nature inspiring us to think along these lines are the gecko feet. More precisely, the Tokay gecko has received a lot of attention in scientific studies aiming to unravel the underlying mechanism of its “togglable” adhesion properties. Although geckos can produce large adhesive forces, they retain the ability to remove their feet from an attachment surface at will [5]. This makes the gecko able to achieve a high adhesion on the feet when climbing a vertical surface while lifting it for the next step remains relatively effortless. For a grasping robot, we might consider an analog frictional concept of a surface material that can change from slippery to rough on demand depending on specific tasks.

In recent years an increasing amount of interest has gone into the studies of the microscopic origin of friction, due to the increased possibilities in surface preparation and the development of nanoscale experimental methods. Nano-friction is also of great concern for the field of nano-machining where the frictional properties between the tool and the workpiece dictate machining characteristics [3]. With concurrent progress in computational power and development of Molecular Dynamics (MD), numerical investigations serve as an invaluable tool for getting insight into the nanoscale mechanics associated with friction. This simulation-based approach can be considered as a “numerical experiment” enabling us to create and probe a variety of high-complexity systems which are still out of reach for modern experimental methods.

In materials science such MD-based numerical studies have been used to explore the concept of so-called *metamaterials* where material compositions are designed meticulously to enhance certain physical properties [6–11]. This is often achieved either by intertwining different material types or removing certain regions completely.

In recent papers by Hanakata et al. [6](2018) [7](2020) numerical studies have showcased that the mechanical properties of a graphene sheet, yield stress and yield strain, can be altered through the introduction of so-called *kirigami* inspired cuts into the sheet. Kirigami is a variation of origami where the paper is cut additionally to being folded. While these methods originate as an art form, aiming to produce various artistic objects, they have proven to be applicable in a wide range of fields such as optics, physics, biology, chemistry and engineering [12]. Various forms of stimuli enable direct 2D to 3D transformations through folding, bending, and twisting of microstructures. While original human designs have contributed to specific scientific applications in the past, the future of this field is highly driven by the question of how to generate new designs optimized for certain physical properties. However, the complexity of such systems and the associated design space make for seemingly intractable problems ruling out analytic solutions.

Earlier architecture design approaches such as bioinspiration, looking at gecko feet for instance, and Edisonian, based on trial and error, generally rely on prior knowledge and an experienced designer [9]. While the Edisonian approach is certainly more feasible through numerical studies than real-world experiments, the number of combinations in the design space rather quickly becomes too large for a systematic search, even when considering the simulation time on modern-day hardware. However, this computational time constraint can be relaxed by the use of machine learning (ML) which has proven successful in the establishment of a mapping from the design space to physical properties of interest. This gives rise to two new styles of design approaches: One, by utilizing the prediction from a trained network we can skip the MD simulations altogether resulting in an *accelerated search* of designs. This can be further improved by guiding the search accordingly to the most promising candidates, for instance, as done with the *genetic algorithm* which suggests new designs based on mutation and crossing of the best candidates so far. Another more sophisticated approach is through generative methods such as *Generative Adversarial Networks* (GAN) or diffusion models used in state-of-the-art AI systems such as OpenAI's DALL-E2 or Midjourney [SOURCE?](#) By working with a so-called *encoder-decoder* network structure, one can build a model that reverses the prediction process. That is, the model predicts a design from a set of physical target properties. In the papers by Hanakata et al. both the *accelerated search* and the *inverse design* approach was proven successful to create novel metamaterial kirigami designs with the graphene sheet.

Hanakata et al. attribute the variety in yield properties to the non-linear effects arising from the out-of-plane buckling of the sheet. Since it is generally accepted that the surface roughness is of great importance for frictional properties it can be hypothesized that the kirigami cut and stretch procedure can also be exploited for the design of frictional metamaterials. For certain designs, we might hope to find a relationship between the stretching of the sheet and frictional properties. If significant, this could give rise to a control of friction behavior beyond manufacturing. For instance, the grasping robot might apply such a material as artificial skin for which stretching or relaxing of the surface could result in a changeable friction strength; Slippery and smooth when interacting with people and rough and firmly gripping when moving heavy objects. In addition, a possible coupling between stretch and the normal load through a nanomachine design would allow for an altered friction coefficient. This invites the idea of non-linear friction coefficients which might in theory also take on negative values given the right response from stretching. The latter would constitute a rarely found property. This has ([only?](#)) been reported indirectly for bulk graphite by Deng et al. [13] where the friction kept increasing during the unloading phase. [Check for other cases and what I can really say here.](#)

To the best of our knowledge, kirigami has not yet been implemented to alter the frictional properties of a nanoscale system. However, in a recent paper by Liefferink et al. [14](2021) it is reported that macroscale kirigami can be used to dynamically control the macroscale roughness of a surface through stretching which was used to change the frictional coefficient by more than one order of magnitude. This supports the idea that kirigami designs can be used to alter friction, but we believe that taking this concept to the nanoscale regime would involve a different set of underlying mechanisms and thus contribute to new insight in this field.

1.2 Goals

In this thesis we investigate the possibility to alter and control the frictional properties of a graphene sheet through application of kirigami inspired cuts and stretching of the sheet. With the use of MD simulations we evaluate the friction properties under different physical conditions in order to get insight into the prospects of this field. By evaluating variations of two kirigami inspired patterns and a series of random walk generated patterns we create a dataset containing information of the frictional properties associated with each design under different load and stretch conditions. We apply ML to the dataset and use an accelerated search approach to

optimize for different properties of interest. The subtask of the thesis are presented more comprehensively in the following.

1. Define a sheet indexing that allows for an unique mapping of patterns between a hexagonal graphene lattice representation to a matrix representation suited for numerical analysis.
2. Design a MD simulation procedure to evaluate the frictional properties of a given graphene sheet under specified physical conditions such as load, stretch, temperature etc.
3. Find and implement suitable kirigami patterns which exhibit out-of-plane buckling under tensile load. This includes the creation of a framework for creating variations within each pattern class. Additionally create a procedure for generating different styles of random walk patterns.
4. Perform a pilot study of a representative subset of patterns in order to determine appropriate simulation parameters to use for the further study along with an analysis of the frictional properties shown in the subset.
5. Create a dataset consisting of the chosen kirigami variations and random walk patterns and analyse data trends.
6. Train a neural network to map from the design space to physical properties such as mean friction, maximum friction, contact area etc. and evaluate the performance.
7. Perform an accelerated search optimizing for interesting frictional properties using the ML model. This should be done both through the pattern generation procedures and by following a genetic algorithm approach.
8. Use the most promising candidtes from the accelerated search to investigate the prospects of creating a nanomachine setup which exhibits a negative friction coefficient.
9. Study certain designs of interest with the scope of revealing underling mechanism. This includes simple correlation analysis but also a visualization of feature and gradient maps of the ML network.

Is the list of subtask to specific? Some of the details here might be better suited for the thesis structure section.

1.3 Contributions

What did I actually achieve

1.4 Thesis structure

How is the thesis structured.

Part I

Background Theory

Part II

Simulations

Chapter 2

Pilot study

Having defined our system, we carry out an initial study of the numerical approach. This includes an analysis of how to define and measure the frictional properties of interest, and an investigation of the main parameters governing the numerical solutions. From this point of view we decide on suitable parameters for the remaining study. Particularly, we investigate the frictional behaviour under the variation of load and stretch for a selected set of configurations which serves as a baseline for later comparison and an assessment of the prospects of Kirigami modifications for friction.

2.1 Friction simulation parameters

The MD simulation is governed by a small set of parameters, some which are related directly to the numerical aspects of the simulation and other related to the physical conditions we are simulating. Thus, we differentiate between the two main categories: 1) *Physical*, parameters which alter the physical conditions of the “numerical experiment” and are expected to effect the frictional behaviour. 2) *Numerical*, parameters which are related more closely to the numerical procedure itself, expected to influence the simulation dynamics, which should be chosen to ensure the most stable results. For the purpose of creating the machine learning dataset most of these parameters will be kept constant with only a subset of the physical parameters being varied. The parameters are summarized in Table 2.1 where the grey shaded area marks the parameters, Configuration, stretch and load, which we will vary for the dataset. Due to the great number of parameters it is unreasonable to make an exhaustive search of all parameters before deciding on the final settings. Instead, we take a basis in the parameters used in similar studies **SOURCES** and adjust them as we carry out the initial analysis of the simulation results. Thus, we start at values most representative for other similar simulations and adjust according to the stability of the results and the computation time. Since we are going to introduce a lot of complexity to the system, through the cut and stretch deformation, we are less concerned about aligning parameters for comparison. Instead of presenting the process of narrowing down the final parameters in a chronological manner, we have shown the final choice shown in Table 2.1 which we will discuss throughout the following presentation of the pilot study. Notice, that the values in Table 2.1 serves as default values which are used when nothing else is stated.

Table 2.1: Parameters of the numerical MD simulation for measuring friction. The values correspond to the final choice used for the dataset. The shaded area denote the parameters varied in the ML dataset.

Category	Parameter	Value	Description
Physical	T	300 K	Temperature.
	v_{slide}	20 m/s	Sliding speed for the sheet translation.
	K	inf	Spring constant for the coupling between the virtuel atom and the sheet pull blocks.
	Scan direction	$(x, y) = (0, 1)$ (zigzag direction)	The direction for which we translate the sheet.
	Sheet configuration	Contiguous	Binary mapping describing which atoms are removed (0) and which is still present (1) in the graphene sheet.
	Stretch amount	0% - rupture	The relative stretch of the sheet.
	F_N	[0.1, 10] nN	Applied normal force to the pull blocks.
Numerical	dt	1 fs	Integration timestep.
	t_R	15 ps	Relaxtion time before strething.
	Pauses	5 ps	Relaxtion pauses after stretch, and during the normal load phase (before translating the sheet).
	Stretch Speed	0.01 ps^{-1}	The rate of stretching for the sheet.
	Slide distance	400 Å	How far to translate the sheet.
	Sheet size	$130.029 \times 163.219 \text{ Å}$	Spatial 2D size of the sheet.
	Pull block size	$2 \times 130.029 \times 15.183 \text{ Å}$	Spatial 2D size of the pull blocks.

2.2 Force traces

We begin by assessing the friction force traces, i.e. force vs. time curves, for a single friction simulation using the default parameters shown in ?? for a non-cut sheet with no stretch applied and a normal load of 1 nN.

2.2.1 Force oscillations

We evaluate the friction force as the force acting on the sheet from the substrate. We consider initially the force componenet F_{\parallel} parallel to the drag direction as plotted in Fig. 2.1. We use a sample rate of $10 \text{ ps}^{-1} = 100 \text{ timesteps}^{-1}$ for which each sample is the mean value of the preceding 100 timesteps. We observe immediately that the data carriers oscillations on different time scales matching our general expectations for sliding involving periodic surfaces. By applying a savgol filter to the data with a polyorder of 5 and window length of 150 timesteps (corresponding to a sliding distance of 3 Å or a time window of 15 ps) we can qualitatively point out at least two different frequencies of oscilation. During the first 10 Å of sliding, seen in Fig. 2.1a, we see roughly three waves on the savgol filter corresponding to a relative high frequency, while for the duration of 100 Å of sliding, seen in Fig. 2.1b, the same savgol filter reveals a lower frequency on top, creating the visual pattern of a wavepacket. The data does not indicate clear signs of stick-slip behaviour as otherwise found in other studies, e.g. by Zhu and Li [15] for graphene on gold, who saw a more typical saw tooth shape in the force trace. Beside the difference in substrate material, using gold instead of silicon, they used a lower sliding speed of 10 m/s and a soft spring of $K = 10 \text{ N/m}$. By adopting those parameters we get a slightly different force trace behaviour as shown in Fig. 2.1c and Fig. 2.1d. This change breaks the symmetry in the force oscillations, but still does not produce any significant discontinuities in the trace. By keeping the spring constant $K = 10 \text{ N/m}$ and lowering the sliding speed further down to 1 m/s we are able to demonstrate a proper stick-slip behaviour as shown in Fig. 2.1e and Fig. 2.1f. Considering all three simulations we might classify the results from the default settings, $K = \text{inf}, v = 20 \text{ m/s}$, as smooth sliding, $K = 10 \text{ N/m}, v = 10 \text{ m/s}$, as a transistion phase with possible occasional slipping, and $K = 10 \text{ N/m}, v = 1 \text{ m/s}$ as certain stick-slip behaviour.

Refer a bit to theory on this one

However, the low sliding speed comes with a high computational cost which is the reason that we choose a sliding speed of 20 m/s. The choice of an infinite spring constant is related to the stability of the measurements as discussed later [make reference](#).

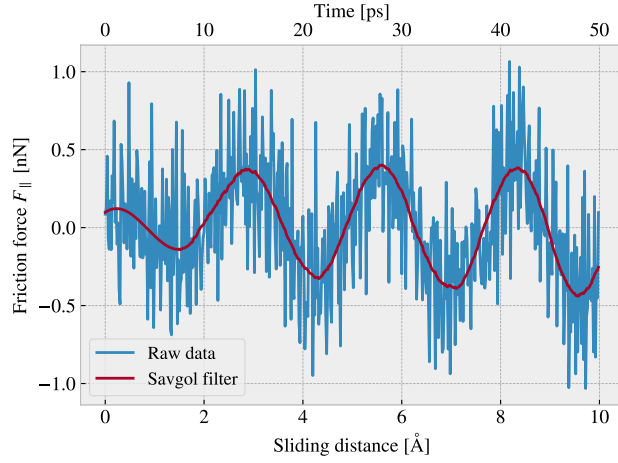
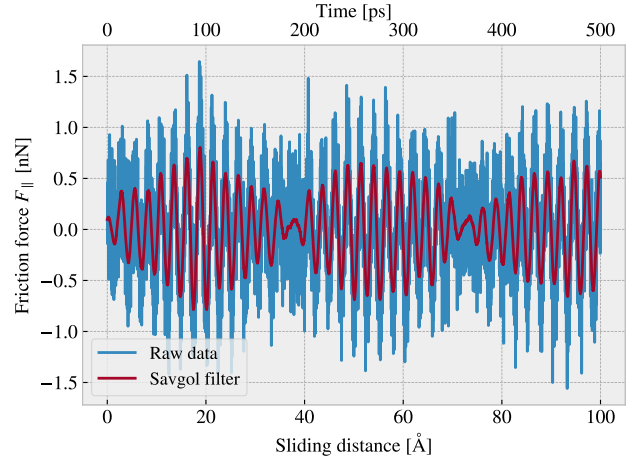
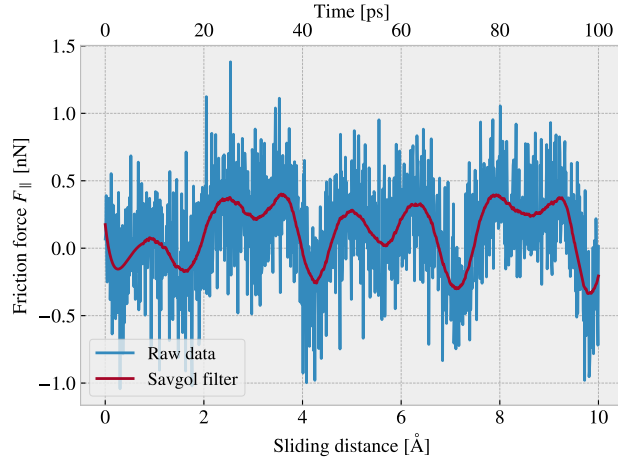
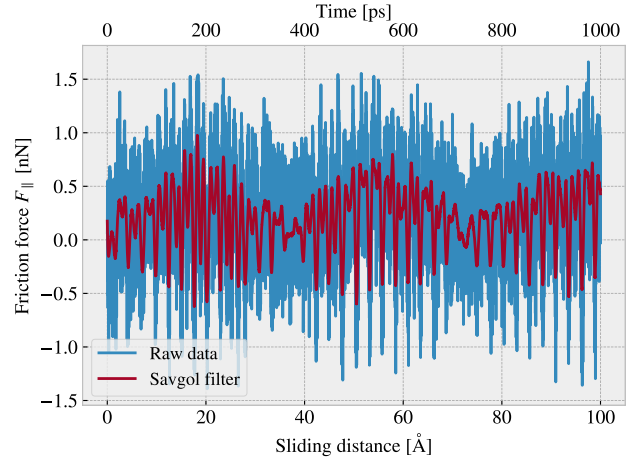
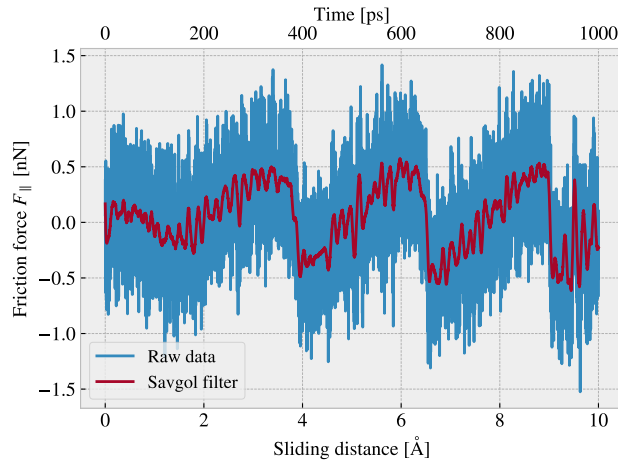
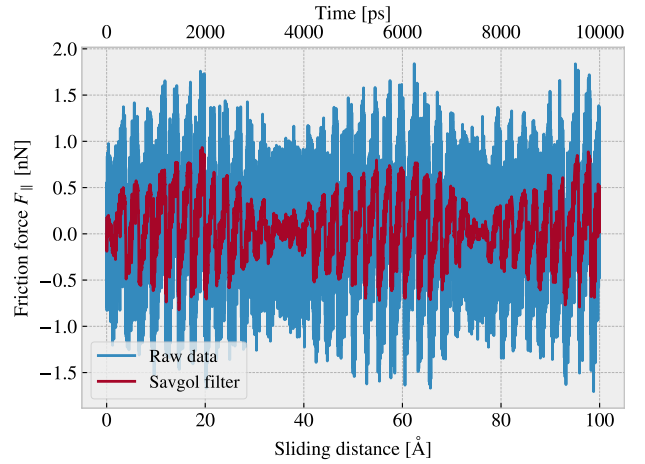
(a) $K = \text{inf}$, $v = 20 \frac{\text{m}}{\text{s}}$ (10 Å sliding).(b) $K = \text{inf}$, $v = 20 \frac{\text{m}}{\text{s}}$ (100 Å sliding).(c) $K = 10 \frac{\text{N}}{\text{m}}$, $v = 10 \frac{\text{m}}{\text{s}}$ (10 Å sliding).(d) $K = 10 \frac{\text{N}}{\text{m}}$, $v = 10 \frac{\text{m}}{\text{s}}$ (100 Å sliding).(e) $K = 10 \frac{\text{N}}{\text{m}}$, $v = 1 \frac{\text{m}}{\text{s}}$ (10 Å sliding).(f) $K = 10 \frac{\text{N}}{\text{m}}$, $v = 1 \frac{\text{m}}{\text{s}}$ (100 Å sliding).

Figure 2.1: Force traces of the friction force F_{\parallel} with respect to the drag direction between acting from the substrate on the full sheet and substrate. The force traces is plotted against the sliding distance (lower x-axis) and the corresponding sliding time (upper x-axis). The sliding distance is measured by displacement of the virtual atom tethering the sheet. The red line represents a savgol filter with window polyorder 5 and window length of 150 timesteps (corresponding to a sliding distance of 3 Å or a time window of 15 ps). Each row, (a,b), (c,d), (e,f), represents a different choice of the spring constant K and sliding speed v , while the columns show the same result for two different time scales. The default settings are represented in figure (a) and (b).

By performing a Fourier Transform on the data, using the default parameters, we can quantify the leading frequencies observed in figure Fig. 2.1a and Fig. 2.1b. The Fourier transform is shown in Fig. 2.2a, and by plotting the two most dominant frequencies $f_1 = 0.0074 \text{ ps}^{-1}$ and $f_2 = 0.0079 \text{ ps}^{-1}$ as a sine sum, $\sin(2\pi f_1) + \sin(2\pi f_2)$, we find a qualitatively convincing fit to the observed wavepacket shape as seen in Fig. 2.2b. We can convert the frequencies according to that of a wavepacket. By using the trigonometric identity

$$\begin{aligned}\sin(a + b) &= \sin(a) \cos(b) + \cos(a) \sin(b), \\ \sin(a - b) &= \sin(a) \cos(b) - \cos(a) \sin(b),\end{aligned}$$

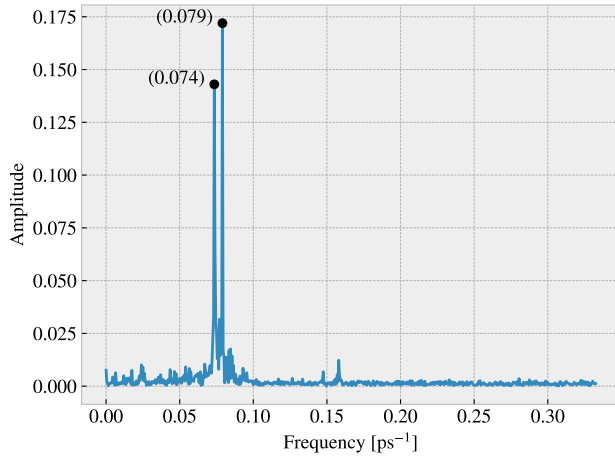
and decomposing the frequencies as $f_1 = a - b$, $f_2 = a + b$, we can rewrite the sine sum as the sinusoidal product

$$\begin{aligned}\sin(2\pi f_1) + \sin(2\pi f_2) &= \sin(2\pi(a - b)) + \sin(2\pi(a + b)) \\ &= \sin(2\pi a) \cos(2\pi b) + \cancel{\cos(2\pi a) \sin(2\pi b)} + \sin(2\pi a) \cos(2\pi b) - \cancel{\cos(2\pi a) \sin(2\pi b)} \\ &= 2 \sin(2\pi a) \cos(2\pi b),\end{aligned}$$

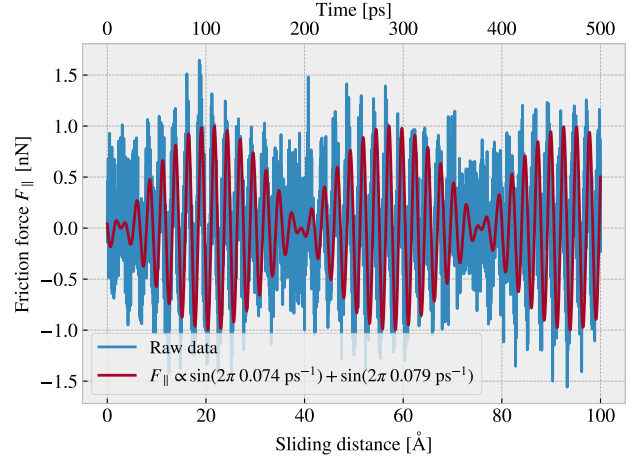
with

$$\begin{aligned}a = \frac{f_1 + f_2}{2} &= 0.0763 \pm 0.0005 \text{ ps}^{-1}, & b = \frac{f_2 - f_1}{2} &= 0.0028 \pm 0.0005 \text{ ps}^{-1}, \\ &= 0.381 \pm 0.003 \text{ \AA}^{-1}, & &= 0.014 \pm 0.003 \text{ \AA}^{-1},\end{aligned}$$

where the latter frequency is denoted with respect to the sliding distance. This makes us recognize the high oscillation frequency as a and the low frequency as b . The faster one has a period of $T_a = 2.62 \pm 0.02 \text{ \AA}^{-1}$ which corresponds well with the magnitude of the lattice spacing and especially that of graphene at 2.46 \AA as expected theoretically. The longer period $T_b = 71 \pm 15 \text{ \AA}^{-1}$ is not obviously explained. We noticed a similar long period oscillation for all three cases, Fig. 2.1b, Fig. 2.1d and Fig. 2.1f, regarding stick-slip behaviour, and thus we not believe that this is directly related. The initial build up in friction force is reminiscent of a friction strengthening, which is often reported [SOURCE](#), but the periodicity goes against this idea. Instead, we might attribute it to some kind of phonon resonance which could be a physical phenomenon or simply a feature of our MD modelling.



(a) FT result shown for a reduced frequency range.



(b) Two most dominant frequencies applied to the data from Fig. 2.1b

Figure 2.2: Fourier transform analysis of the full friction force data (all 400 \AA sliding distance) shown in Fig. 2.1. (a) shows the two most dominant frequency peaks. Note that no significant peaks was found in a higher frequency than included here. (b) shows a comparison between the raw data and the wavefunction corresponding to the two peaks in figure (a).

¹The uncertainty Δy is calculated as $\Delta y = \left| \frac{\partial y}{\partial x} \Delta x \right|$ for uncertainty Δx and $y(x)$

2.2.2 Decompositions

In the previous analysis we have looked only at the friction force for the full sheet, including the rigid pull blocks, and with respect to the drag direction. We found this way of measuring the friction force to be the most intuitive and reliable, but we will present the underlying arguments for this choice in the following.

Due to the fact that we are only applying cuts to the inner sheet, and not the pull blocks, it might seem more natural to only consider the friction on that part. If the desired frictional properties can be achieved by altering the inner sheet one can argue that any opposing effects from the pull blocks can be mitigated by simply scaling the relative size between the inner sheet and the pull blocks. However, when looking at the force traces decomposed with respect to the inner sheet and pull block regions respectively, see Fig. 2.3a, we observe that the friction force arising from those parts are seemingly antisymmetric. That is, the distribution of the frictional pull from the substrate on the sheet is oscillating between the inner sheet and the pull block. Keeping in mind that normal force is only applied to the pull blocks we might take this as an intrinsic feature of the system which does not necessarily disappear by scaling of the spatial ratio between the inner sheet and pull block. Any interesting friction properties might depend on this internal distribution of forces. Hence, we hedge our bets and use the full sheet friction force as a holistic approach to avoid excluding relevant information in the measurement data.

Similar we might question the decision of only considering the frictional force projected onto the sliding direction as we are then neglecting the “side shift” induced during sliding. In Fig. 2.3b we show the decomposition in terms of force components parallel F_{\parallel} and perpendicular F_{\perp} to the sliding direction respectively. We notice that the most dominant trend appears for the parallel component. If we want to include the perpendicular component as well we would have to evaluate friction as the length of the force vector instead, but this would remove the sign of the force direction and shift the mean friction force up as we clearly see both negative and positive contributions in the parallel force trace. One option to accommodate this issue is by using the vector length for the magnitude but keeping the sign from the parallel component. However, we omit such compromises as this might make the measurement interpretation unnecessarily complex, and we use only the parallel component going forward.

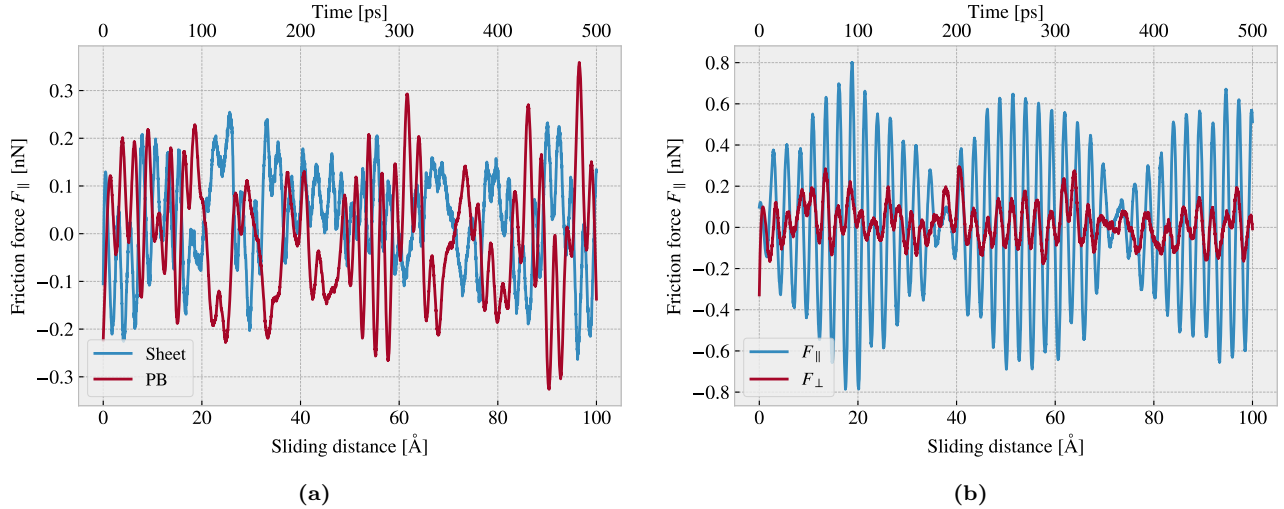


Figure 2.3: Friction force decomposition on the default parameter force trace shown in Fig. 2.1 showing only the applied savgol filters. (a) Decomposition into group inner sheet (sheet) and pull blocks (PB). (b) Decomposition into parallel (F_{\parallel}) and perpendicular (F_{\perp}) to drag sliding direction.

2.2.3 Center of mass path

From the previous observations of the force traces Fig. 2.1 we demonstrated both smooth sliding and stick-slip behaviour. Considering the force decomposition in Fig. 2.3b we know that the frictional forces in the perpendicular direction to sliding is also present. By looking at the x, y -position for the sheet Center of Mass (CM) we see a qualitative different behaviour when reconsidering the spring constant and sliding speed investigated in Fig. 2.1 which is shown in Fig. 2.4. The default case in Fig. 2.4a shows a rather straight path forward with only a

small side motion in comparison to the cases in Fig. 2.4b and Fig. 2.4c. However, the CM accelerates and deaccelerates with a high frequency, much too high to be associated with the lattice spacing on the order of 2.46 Å (interatomic distance of 1.42 Å). One possible explanation is that the sheet and substrate constitutes an incommensurable contact for which travelling kink excitations make the atoms move in such a way that the sheet CM is incremented in small “burst”. When looking at the $K = 10 \frac{\text{N}}{\text{m}}$, $v = 10 \frac{\text{m}}{\text{s}}$ case in Fig. 2.4b we see a completely different CM path where the rapid parts aligns visually better with the force oscillations shown earlier in Fig. 2.1d. The CM accelerates forward and the deaccelerates in combination with a side motion that lead to the CM path making a loop as it slows down. Finally we have the $K = 10 \frac{\text{N}}{\text{m}}$, $v = 10 \frac{\text{m}}{\text{s}}$ in Fig. 2.4b which is confirmed to have stick-slip behaviour in Fig. 2.1f. Here the CM path shows a more chaotic movement between acceleration which also alligns visually well with the timing of the slips seen in Fig. 2.1f. The chaotic motion is not obviously connected to the stick-slip motion, but we omit a further investigation as this is not corresponding to the parameters that we will be using.

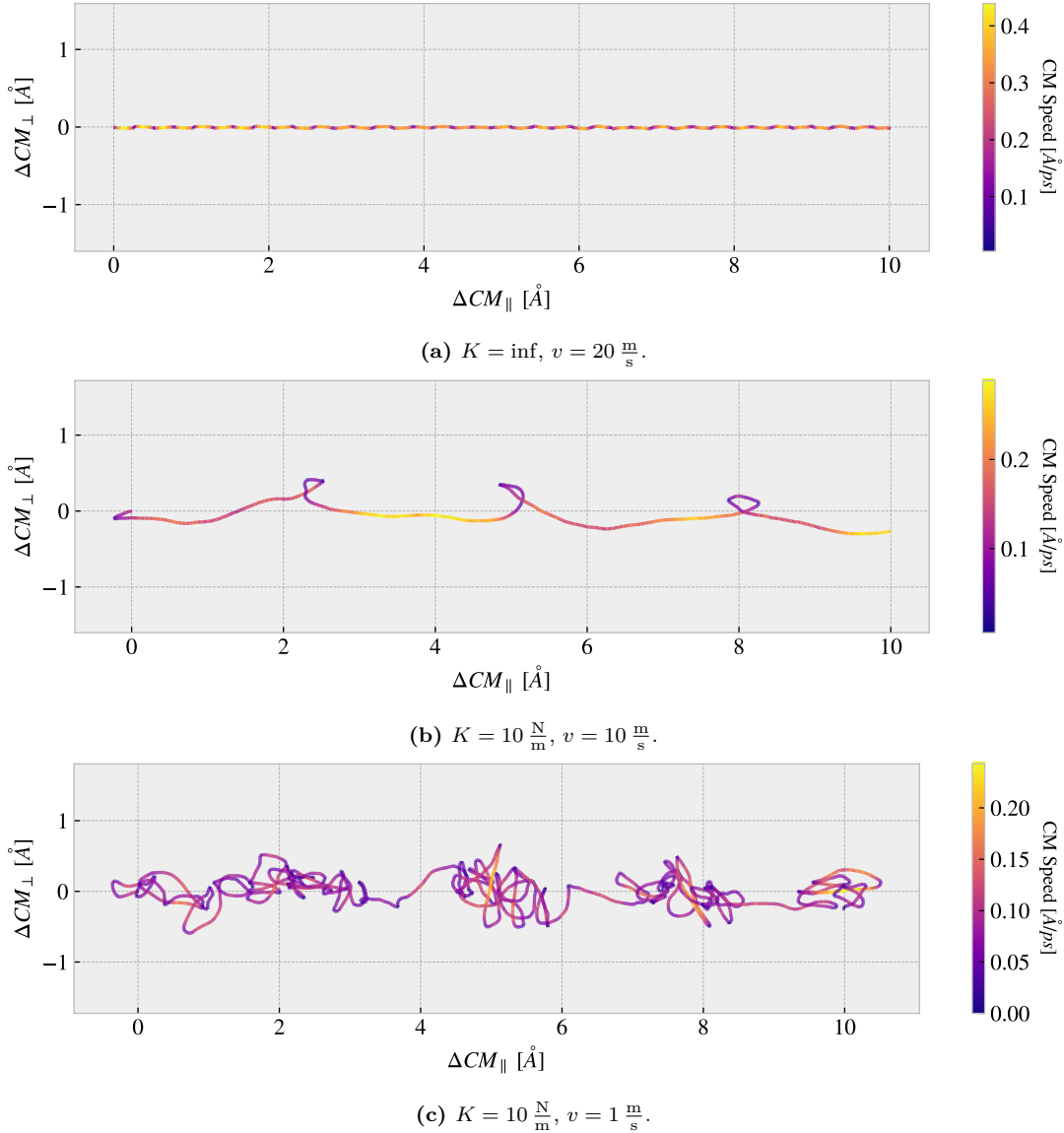


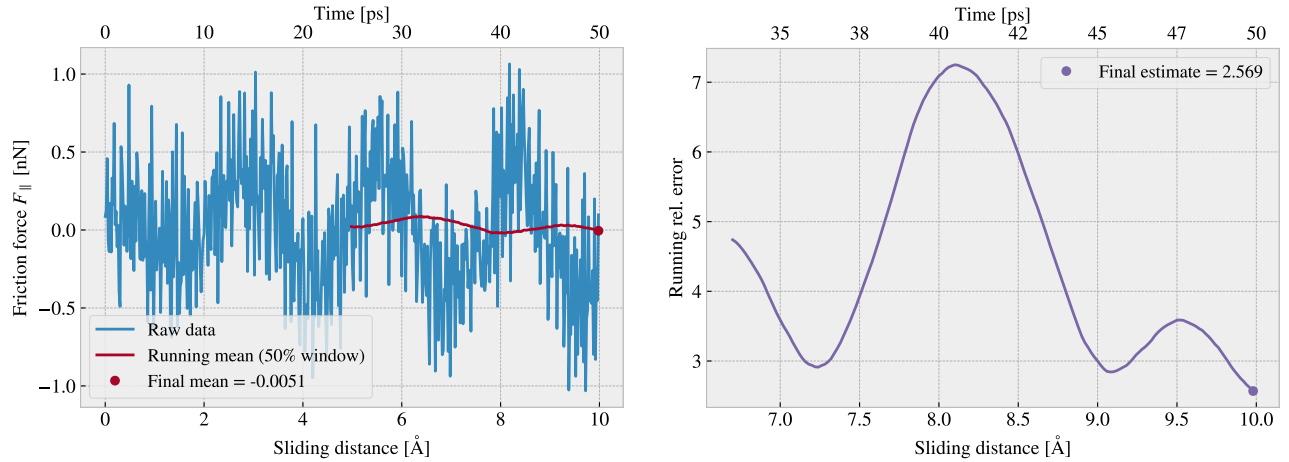
Figure 2.4: Center of Mass (CM) position relative to the start of the sliding phase in terms of the direction parallel to the sliding direction $\Delta COM_{||}$ and the axis perpendicular to the sliding direction ΔCOM_{\perp} . The colorbar denotes the absolute speed of the CM motion. Figure a-c shows different parameters used for the spring constant K and sliding speed v similar to that used in Fig. 2.1. (a) Default: $K = \text{inf}$, $v = 20 \frac{\text{m}}{\text{s}}$. (b) $K = 10 \frac{\text{N}}{\text{m}}$, $v = 10 \frac{\text{m}}{\text{s}}$. (c) $K = 10 \frac{\text{N}}{\text{m}}$, $v = 1 \frac{\text{m}}{\text{s}}$.

2.3 Defining metrics for friction

In order to evaluate the frictional properties of the sheet we aim to reduce the force trace results, addressed in section Sec. 2.2, into single metrics describing the kinetic and static friction respectively.

2.3.1 Kinetic friction

We measure kinetic friction as the mean of the friction force trace. More precisely, we take the mean value of the latter half of the dataset in order to ensure that we are sampling from a stable system. For a full sliding simulation of 400 Å we thus base our mean value on the latter 200 Å (1000 ps) of sliding. In Fig. 2.5a we have shown the force trace for the first 10 Å of sliding together with a 50% running mean window. The choice of such a short sliding distance is merely to illustrate the sampling procedure, and we see that the final mean estimate (marked with a dot) takes a negative value due to the specific cut-off of the few oscillation captured here. Nonetheless, one approach to quantify the uncertainty of the final mean estimate is to consider the variation of the running mean preceding the final mean value. The more the running mean fluctuates the more uncertainty associated with the final estimate. Only the running mean “close” to the ending should be considered, since the first part will rely on data from the beginning of the simulation. From the Fourier analyse in section Sec. 2.2.1 we found the longest significant oscillation period to be $\sim 71 \text{ Å}^{-1}$ corresponding to $\sim 35\%$ of the running mean window which gives a window length of 200 Å when including all the data. Hence, we use the standard deviation of the final 35% of the running mean to approximate the uncertainty of the final mean value. We consider the standard deviation (std) as an estimate of the absolute error and calculate the relative error by a division of the final mean value. In Fig. 2.5b we showcase a running relative error based on the std, with a window of length 35% the mean window, in a continuation of the illustrative case of a 10 Å sliding from Fig. 2.5a. In this case we get an extremely high relative error of $\sim 257\%$, but this is desirable since the sampling period leads to an unphysical negative value which should be associated with a high uncertainty.



(a) Running mean with window length 5 Å (50% the data length). (b) Running std with window length 1.75 Å (35% the mean window length.)

Figure 2.5: Running mean (a) and running relative error (std) (b) on the friction force data from a reduced sliding distance of 10 Å. The running mean window is 50% the data length while the running std window is 35% the running mean window length. The values are plotted at the end of their respective windows such that window precedes the actual point on the graph.

When including the full dataset of 400 Å of sliding, such that the std window actually matches with the longest period of oscillations expected, we get a final relative error of $\sim 12\%$ as shown in fig Fig. 2.6. This is arguable just at the limit of an acceptable error, but as we shall see later on in Sec. 2.6 this high relative error is mainly associated with the cases of low friction. When investigating different configurations under variation of load and stretch we see a considerable lower relative error as the mean friction evaluates to higher values. One interpretation of this finding is simply that the oscillations in the running mean are to some degree independent of

the magnitude of the friction. In that case, the relative error will spike for the low friction cases, and the absolute error might be there more reliable measure, i.e. taken simple the std without dividing by the final mean value.

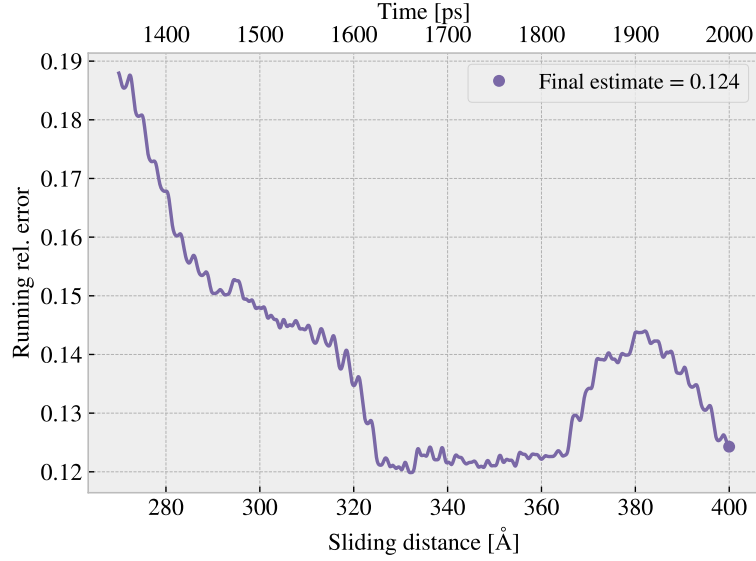


Figure 2.6: Running standard deviation (std) for a full 400 Å sliding simulation. The running std window is 70 Å (35% the running mean window of 50% the data length).

2.3.2 Static friction

The maximum value is one of the comon choices for adresssing static friction, even though the definition of static friction is a bit vague. When considering the force traces in Fig. 2.1 we observe that the force oscillations increase in magnitude toward a global peak at ~ 20 Å. Thus, one could be inclined to identify this peak as the maximum value associated with the static friction force. However, as we have already clarified, this steady increase in friction is a part of a slower oscillation which repeats by a period of ~ 71 Å⁻¹. By plotting the top three max values recorded during a full 400 Å simulation, for 30 logaritmicly spaced load values in the range [0.1, 100] nN, we observe that the global max in fact rarely fall within this first oscillation period as shown in Fig. 2.7. Only 2/30 global maxima and 4/90 top three maxima can be associated to the start of the sliding by this definition. Thus, this result suggest that our default system does not yield a static friction response in the sense of an initial increase in friction due to a depinning of the sheet from the static state **Is this probably definned in the theory section**. Some parameter changes that might increase the likelihood of seeing a significant static friction response is either extending the relaxtion period, as static friction is theorized to increase logarithmically with time, or to increase the sliding force more slowly and through a soft spring tethering. As an attempt to test parts of this hypothesis we run a series of simulations with varying spring constant, $K \in [5, 200]$ nN including also $K = \text{inf}$, but keeping the relaxtion time and sliding speed at the default values. The result is shown in Fig. 2.8. The results do not show any support of the hypothesis that a softning of the spring constant will eventually lead to the maxima occouring in the first periode of sliding. We note that this might be suppressed by having a too short relaxtion period or a too high sliding speed, related to the rate of which force increased initally, but due to the ambiguousness in the assesment of the static friction we will mainly consern ourselves with the kinetic friction in the remaning of this thesis.

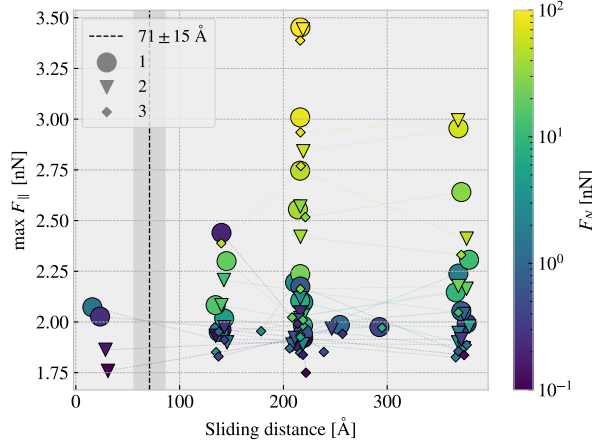


Figure 2.7: Distribution of top three max friction force peaks for 30 uniformly sampled normal forces $F_N \in [0.1, 10]$ nN. The dotted line and the grey area marks the slowest significant oscillation period found in the data and thus marking a dividing line for whether a peak falls within the “beginning” of the sliding simulation.

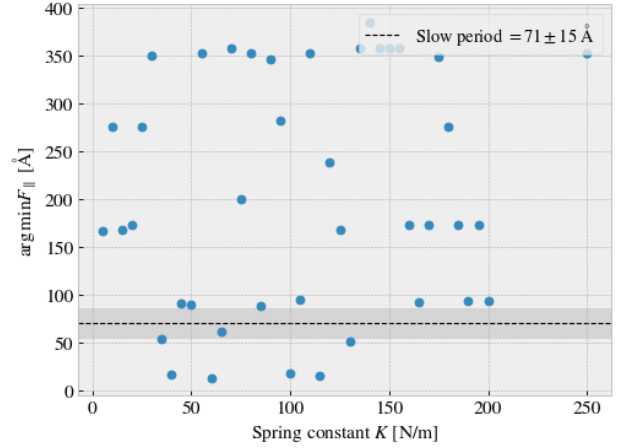


Figure 2.8: Sliding displacement for the max friction peak to appear as a function of spring constant. **Fixmove is tmp mapped to $K = 200$ here without any discontinuous lines.**

2.4 Out-of-plane buckling

The out-of-plane buckling is one of the original motivations for investigating the application of Kirigami cuts in the context of friction properties. Therefore, we perform a stretch simulation, at low temperature ($T = 5$ K) without any substrate, in order to verify that we are able to reproduce an out-of-plane buckling with the intended patterns described in ???. For this investigation we include the non-cut sheet, the Tetrahedron (7, 5, 1) and the Honeycomb (2, 2, 1, 5) pattern. We quantify the out-of-plane buckling by assessing the distribution of atoms along the z-direction (perpendicular to the plane) during stretching. We calculate the minimum and maximum z-value as well as the atom count quartiles 1%, 10%, 25%, 50% (median), 75%, 90% and 99% as shown in figure Fig. 2.9. The results show significant buckling for the Tetrahedron and Honeycomb patterns in comparison to the non-cut sheet which only exhibit minor buckling of ~ 2 Å which is on the same order as the lattice spacing. Moreover, we notice that the Tetrahedron pattern buckles more in consideration to the min. and max. peaks while the remaining quartiles actually seem to be more closely spaced than for the Honeycomb. By addressing the simulation visually, using the Open Visualization Tool OVITO, we find that this can be attributed to fringes on the edge “flapping around” and thus increasing the min. and max. values.

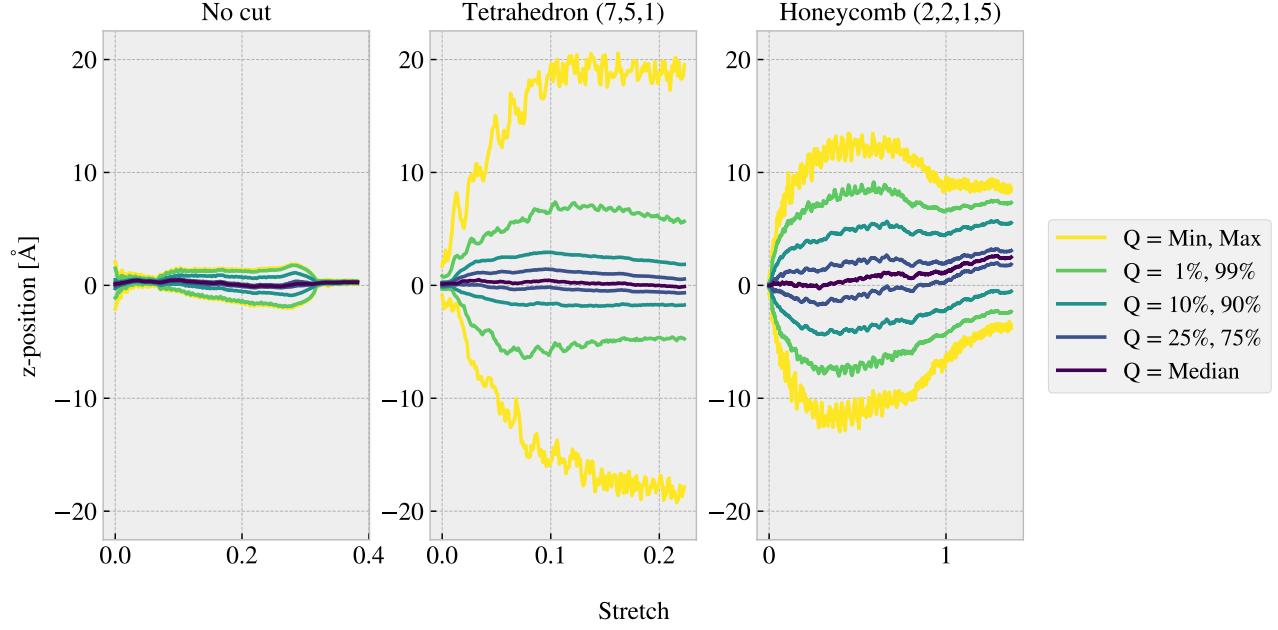


Figure 2.9: Out-of-plane buckling during stretching of the No cut, Tetrahedron (7, 5, 1) and Honeycomb (2, 2, 1, 5) sheet respectively in vacuum at low temperature $T = 5$ K. The buckling is measured by the distribution of the atom z-position (perpendicular to the sheet plane), for which the colors indicates selected quantiles. The yield strain were, reading from left to right, 0.38, 0.22 and 1.37.

Given the confirmation of out-of-plane buckling in a vacuum, as seen in Fig. 2.9, we reintroduce the substrate in order to investigate whether this effect carries over to a change in contact area. We raise the temperature to the default value of $T = 300$ K. We keep the normal force off and let the sheet stick purely by the adhesion forces between the sheet and substrate. We quantify the contact area through the relative amount of atoms in the sheet within chemical range of the substrate. The cut-off for this interaction is set to 4 Å, inspired by [16], corresponding to $\sim 120\%$ the LJ equilibrium distance. Usually the contact area is calculated as the number of contacting atoms multiplied with an associated area for each atom. However, since we are not interested in the absolute value of the actual area, but rather the relative change, we omit the multiplication factor. That is, we consider the relative number of atoms within contact range, which is proportional to the contact area, as our metric of choice. The relative contact for the three configurations (No cut, Tetrahedron (7, 5, 1) and Honeycomb (2, 2, 1, 5)) during stretching are shown in figure Fig. 2.10. The figure reveals a significant drop in contact as the sheets are stretched, which agrees qualitatively with the buckling observed without the substrate (Fig. 2.9). The Honeycomb pattern turns out to be both the most stretchable, with a rupture strain at 127% its original length, and the one with the biggest decrease in relative contact down to approximately 43%. Notice, that the relative contact is never actual 1.0 but instead maxes out at around 96% with no stretching. This is attributed to the temperature fluctuations and the choice of cut-off.

Selected frames from the simulation result are shown in appendix ?? which reveals a bit more information of how the buckling accours. The Tetrahedron pattern deforms rather quickly and smoothly into small tetrahedron spikes, as the name suggest. While the Tetrahedron deformation appeared rather uniformly the Honeycomb pattern deformaitons inniate from one side first. As the sheet stretches more rows of the pattern is activated, producing the honeycomb looking shape when seen from above. As both patterns approaches the rupture point the tensions leads to a small increase in the relative contact again. This agrees with the results in Fig. 2.9 where the buckling reduces slightly towards the end.

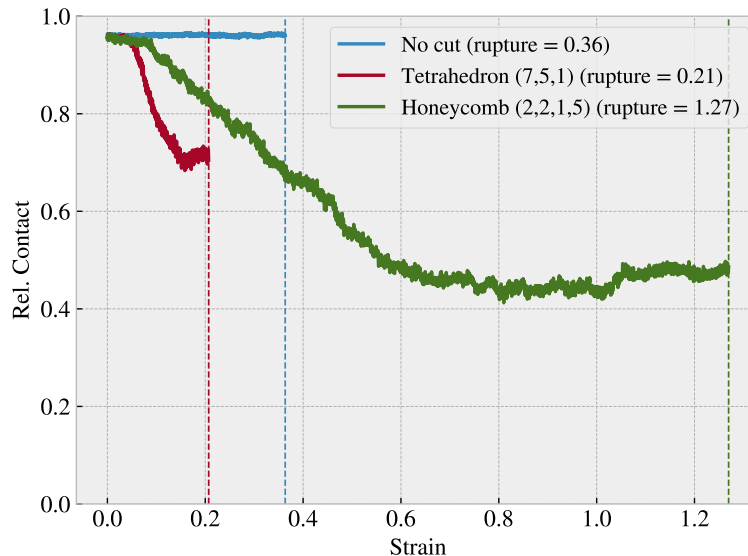


Figure 2.10: Relative contact, given as the relative number of atom in the sheet being within chemical interaction range, vs. strain of the sheet. The cut-off for the interaction range is 4 \AA corresponding to $\sim 120\%$ the LJ equilibrium distance. No normal force is applied and temperature is kept at $T = 300 \text{ K}$.

Compare figure Fig. 2.10 to that of figure ?? where multiple simulations constitute the stretch-contact curve.

2.5 Investigating main parameters

We carry out a more extensive investigation of the dependence on friction of the physical parameters temperature T , sliding speed v_{slide} and spring constant K , and the numerical parameter timestep dt . This is done partly to understand how the dependencies relate to theoretical, numerical and experimental results, and partly to understand how these parameters effects the stability of our system. We use the default parameters presented in ?? and investigate the results as we change a single parameter, one at a time. We keep the load at 1 nN . We consider the mean friction force, sampled from the latter half of the simulation as described in Sec. 2.3, representing the kinetic friction. The results are presented Fig. 2.11. We have indicated the absolute error visually, defined by the std as described in Sec. 2.3, as a shaded area which connects linearly between data points. Generally, we notice that the parameter dependencies differs between the different configurations.

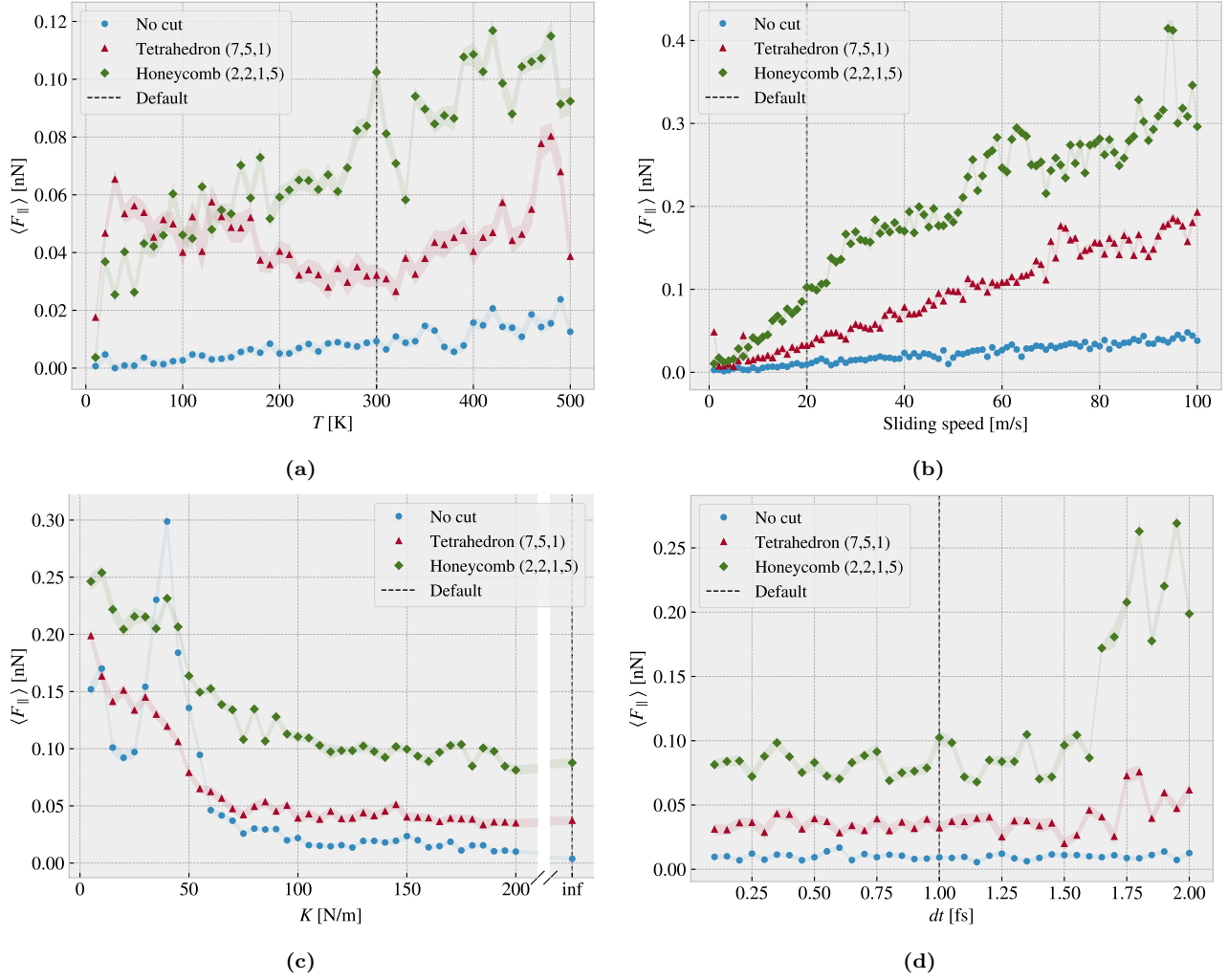


Figure 2.11: Main parameters investigation. Kinetic friction force

From the temperature investigation in Fig. 2.11a we find an increasing kinetic friction with temperature for both the non-cut sheet and the Honeycomb pattern. The Tetrahedron pattern shows both decreasing and increasing trends as it yields an initial rapid (10–30 K), followed by a more slowly decrease (30–320 K), which turns around and increases (320–480 K), and finally a rapid drop decrease again (480–500 K). Similar rapid changes are also seen from the Honeycomb pattern, although the underlying trend is seemingly increasing throughout. We notice that for the non-cut and Honeycomb sheet, which can be attributed some sort of underlying linear increase, the rate of increase is higher for the Honeycomb than the non-cut sheet. From a theoretical and experimental point of view we would expect a decrease in friction with temperature. However, an increasing trend is also observed by Zhang et al. [17] (sliding at 10 m/s) which we associates with a high sliding speed causing ballistic motion [Revisit theory on this one](#). Since the results does not indicate any plateau for which the temperature choice is more or less stable with respect to changes, we have choosen the room temperautre $T = 300$ K

From the sliding speed investigation in Fig. 2.11b we generally find an increasing friction with velocity. Due to the relatively high velocities availble and the effects from the thermostat, we expect a viscous friction $F_k \propto v_{\text{sliding}}$ which matches rather well with these results. However, the Tetrahedron and Honeycomb sheets seem to fall slightly into a sublinear relationship as it approaches higher velocities. Moreover, the cut sheets exhibit some local fluctuations which might be attributed to resosnace effects as discussed with respect to the phonon dynamics. Our choice of sliding speed at 20 m/s mainly reflects a consideration of computational cost, but the fact that no immediate resonance fluctuations appears around this values supports the choice.

From the investigation of the spring constant parameter in Fig. 2.11c we observe a significant decrease in friction as the springs stiffens. This can be attributed to the transition from a stick-slip influenced regime to a smooth sliding regime as we saw for the force traces in Fig. 2.1. For soft springs the result is quite sensitive to the specific choice of spring constant which is especially seen for the non-cut sheet as it peaks at $K = 40 \text{ N/m}$. Thus, in order to avoid such a sensitivity we settled for the infinite stiff spring with the intention of getting more stable results in our configuration investigation.

Finally, we consider the stability of the result as we vary the simulation timestep in Fig. 2.11d. The general trend shows a stable plateau below $\sim 1.5 \text{ fs}$ for which higher values reveal arising instabilities for the cut sheets. This mainly confirms that our choice of timestep is within a reasonable range. However, we do see some fluctuations which are more significant for the cut patterns. These fluctuations can be taken as a sign of the sensitivity to randomness in our simulation. An extended study of the effect of changing the random seed for the initial velocity and thermostat could bring more insight into this matter. However, we might interpret this as an indication that the uncertainty is higher than otherwise estimated by the running mean and running std evaluation. For the Honeycomb sheet the fluctuations are on the order ± 0.017 which corresponds to a relative error of $\sim 20\%$. This number is a bit unsettling, but we take note of this as an upper limit for the error at an unstretched stage.

2.5.1 Computational cost

Say something about how we run the simulations?

As we analyse the numerical and physical dependencies in the system we also consider the computational cost. This especially relates to the parameters defining the total number of computations such as timestep, sliding speed and sliding distance. As an extension of the analysis in Sec. 2.5 we report on the computational times associated with temperature, sliding speed, spring constant and dt . By retrieving the computational time used for the parameter investigation in Fig. 2.11 we get the timing as shown in Fig. 2.12. Note that these timings only give one time estimate for each parameter setting as opposed to an average over multiple runs which is necessary for more reliable data.

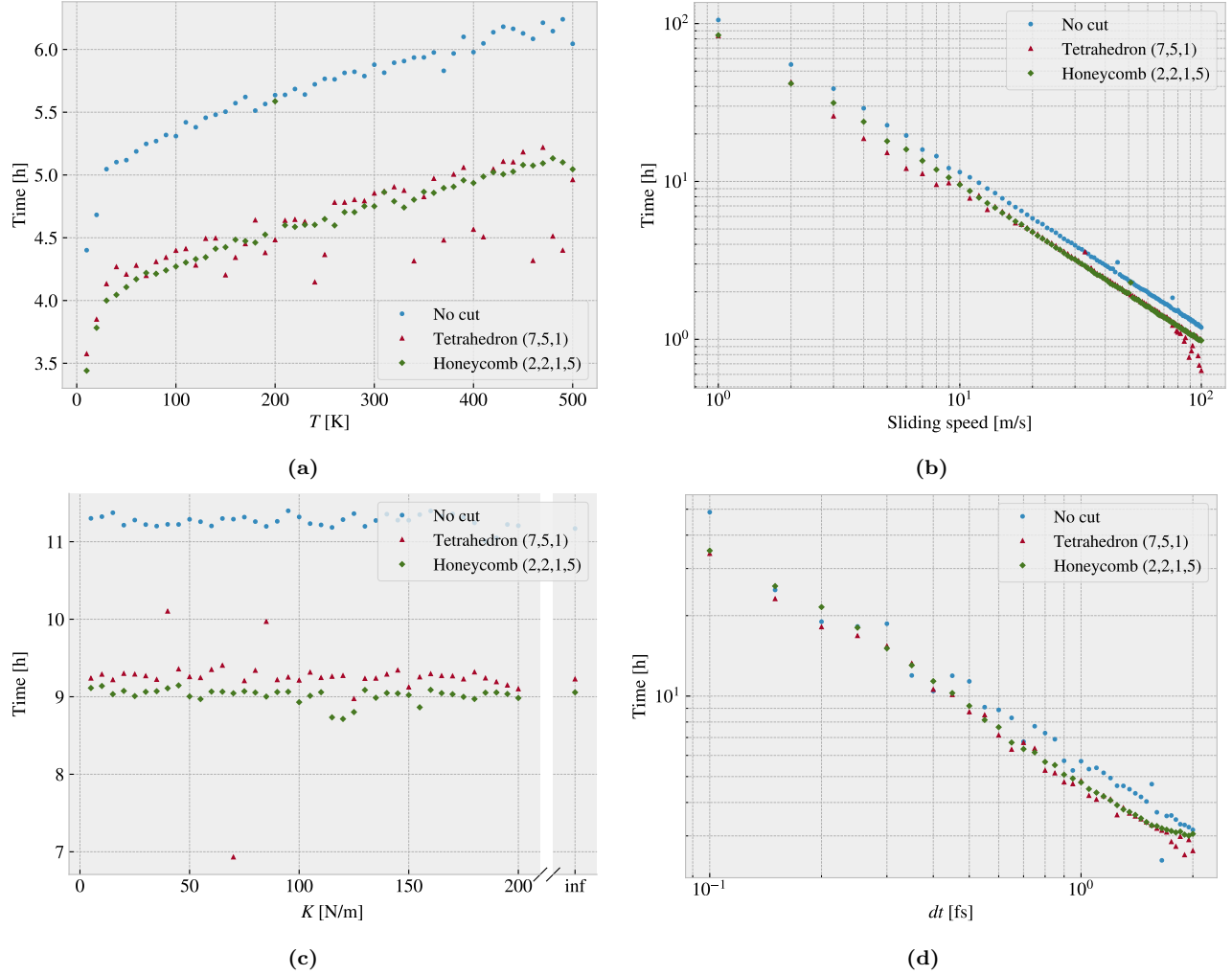


Figure 2.12: Computational cost related to temperature, sliding speed, spring constant and dt parameter in terms of CPU hours running on 16 cores on the cluster [double check and elaborate](#). Sliding speed follows $t \propto v^{-0.977 \pm 0.005}$ and dt follows $t \propto dt^{-0.87 \pm 0.02}$

The computational time is governed by the number of timesteps in the simulation and the time used per timestep. For a fixed sliding distance, which is the case here, the number of timesteps in the simulation should be inversely proportional to sliding speed and similar inversely proportional to timestep dt . From the timings in Fig. 2.12 we find the sliding speed to obey this expectation rather well by $t \propto v^{-0.977 \pm 0.005}$ while the timing did not increase as strongly with timestep, falling below the $1/dt$ relation with $t \propto dt^{-0.87 \pm 0.02}$. Moreover, we find that increasing temperature also makes for an increased computation time. This can be attributed to an increase in computation time associated with the force calculations. The rising temperature gives rise to more fluctuations in the system which might yield more atoms within the force calculation cutoffs. The consideration to cutoff could also be part of the reason for the deviating timing relation for dt . Finally, for the spring parameter, we did not see any noticeable effect on timing.

[Mention system size timing?](#)

2.6 Load and stretch dependencies

So far, we have carried out a general analysis of the system behaviour under different parameters which lays the foundation for the remaining study. We now shift our intention towards the friction dependence of load and stretch.

2.6.1 Pressure reference for normal load

We consider a load range of 0.1–10 nN which alligns with the general choice in other MD studies [SOURCE](#). In order to relate to the magnitude of this load we provide a short calculation of the corresponding pressure. We will use the pressure underneath a stiletto heeled shoe as a high pressure reference from our macroscale world. The diameter of a stiletto heeled shoe can be less than 1 cm [18], and hence an 80 kg man² standing on one stiletto heel, with all the weight on the heel, will correspond to a pressure

$$P = \frac{F}{A} = \frac{mg}{r^2\pi} = \frac{80 \text{ kg} \cdot 9.8 \frac{\text{m}}{\text{s}^2}}{\left(\frac{10^{-2} \text{ m}}{2}\right)^2\pi} = 9.98 \text{ MPa}.$$

The fact that the pressure under a stiletto heel can get this high, actually greater than the pressure under an elephant foot, is in an interesting realization in itself that is often used in introductory physics courses [19], but this also serves as a reasonable upperbound for human executed pressure. With a full sheet area of $\sim 21 \times 10^3 \text{ \AA}^2$ our load range of 0.1–10 nN corresponds to a pressure of 0.47–47 MPa which relates nicely with our macroscale reference. This pressure might be incompatible with various industrial purposes, but with no specific application in mind this serves as a decent reference point. Notice that if we consider a human foot with area 113 cm^2 [20] the pressure drops to a mere 70 kPa corresponding to only $\sim 0.01 \text{ nN}$.

2.6.2 Stretch dependencies

We consider the effects of stretching the sheet using the non-cut. Tetrahedron (7, 5, 1) and Honeycomb (2, 2, 1, 5) sheet as used so far. For each configuration we run a rupture test where the given sheet is stretched under zero load, but still under the influence adhesion from the substrate. The rupture point is then noted such and multiple simulations with different stretch between zero and the rupture limit are run. For the sampling of the stretch values in the available range we use a pseudo uniform distribution, meaning that we divide the given interval in equal segments and pick a value from each segments by a uniform distribution. This is due to numerical limitations in LAMMPS, but we find that this gives evenly spaced values which also carries some randomness. For the load we use 0.1, 1 and 10 nN.

First, we aim to reproduce the contact investigation from Fig. 2.10. We quantify the relative contact as described in Sec. 2.4, but converts this into a single metric for a given simulation by considering the average of the latter 50% of data points, similar to what we have done for the mean friction, and we adopt the same method for quantifying the error. The results are shown in Fig. 2.10 where we observe a significant decrease in contact for the kirigami patterns which qualitatively agrees with the non-loaded continuous stretch investigation from Fig. 2.10. This result implies that the change in contact can not be related to a momentum effect during stretching, as each simulation now keeps the stretching constant. throughout. The absolute error for the mean rel. contact were generally quite low on the order of 0.01 for all configurations.

From an asperity theory point of view this reduction in contact is theorized to induce a similar reduction in friction, but when considering the kinetic friction shown in Fig. 2.13b we find that this is definitely not the case. As the contact decreases, for the Tetrahedron and Honeycomb pattern, the friction increases. Yet, these are not simply inverse proportional as the friction force suddenly dips down and up again, around 0.08–0.11 for the Tetrahedron and 0.73–1.05 for the Honeycomb pattern. This suggests that the contact is not a dominating mechanism for friction in this system. The absolute error were fairly low on the order of 0.001–0.01 nN.

We notice also that the two orders of magnitude increase in normal load did not make a significant difference in the results. In a study by Zhang et al. [21] they found that straining the sheet lead to a reduction in friction. Despite the fact that our result suggest an increase in friction with straining we notice that the observed effect is only present for the kirigami sheets, while the non-cut sheet shows no significantly impact.

Tension does also not seem to be the answer since the non cut sheet does not really change

²Yes, a man can certainly wear stilleto heels.

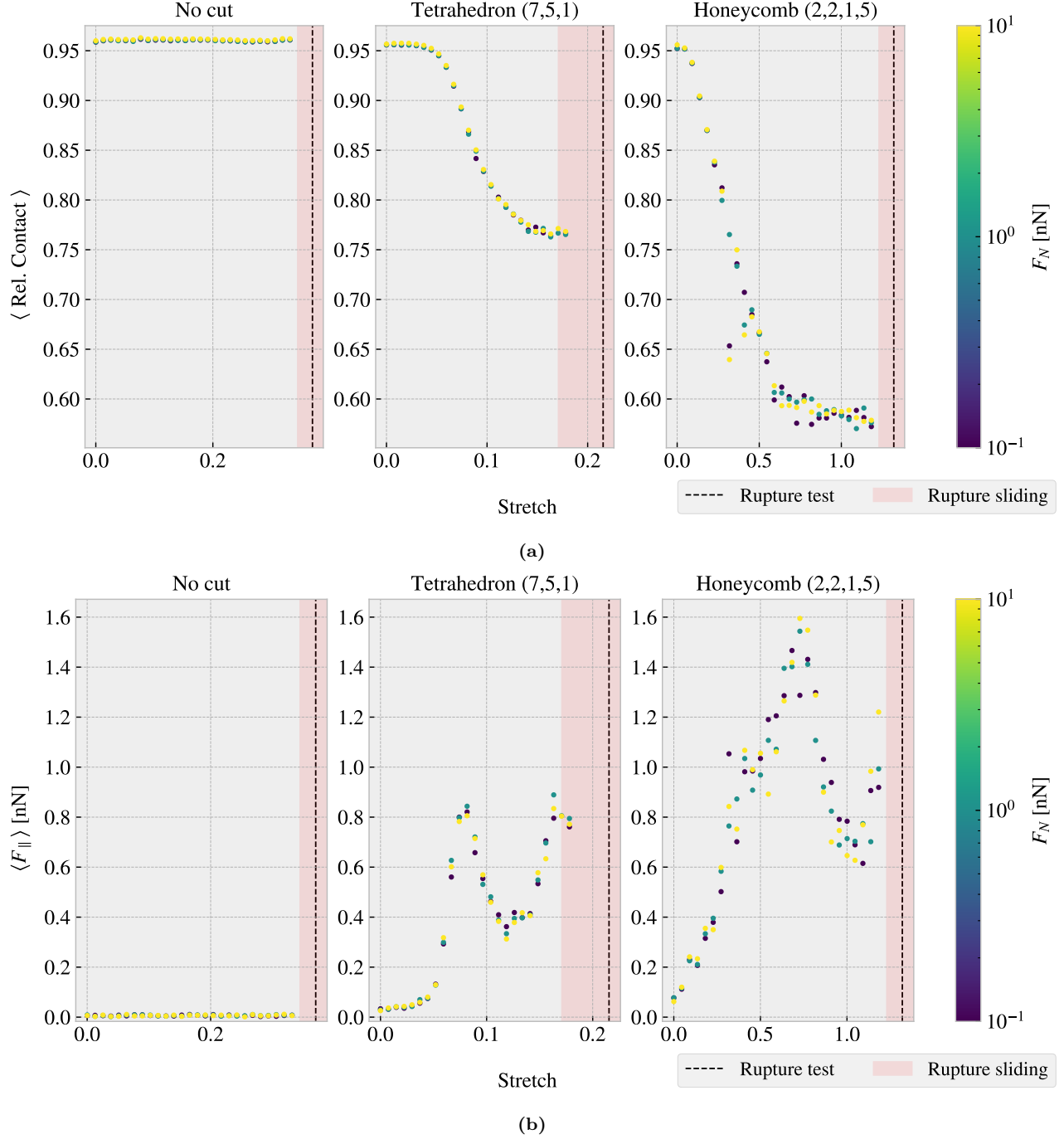


Figure 2.13: Average relative contact and average friction for multiple simulations, consisting of 30 stretch values sampled from a pseudo uniform distribution between 0 and the rupture point in combination with loads 0.1, 1 and 10 nN, for each of the configurations: non-cut, Tetrahedron (7, 5, 1) and Honeycomb (2, 2, 1, 5). The average is taken over the latter half of the sliding phase. The red shade denotes the stretch range where ruptures occurred during sliding while the black-dotted line represent the rupture point in the no load rupture test. (a) The average relative contact defined as the relative number of atoms within a contact threshold of 4 Å to the substrate. The absolute error is on the order 0.01 (b) The average mean friction force parallel to the sliding direction. The absolute error is on the order 0.001–0.01 nN

By considering the increase in friction from no stretch towards the first peak we find that the Tetrahedron pattern exhibit a relative increase of ~ 27.7 while the Honeycomb pattern exhibit a relative increase of ~ 22.4 . This is in itself a remarkable result, but considering that the friction drops almost as dramatically down again is

even more unexpected. These results are thus promising for the prospect of demonstrating a negative friction coefficients by altering the stretch through a coupling to the load.

2.6.3 Load dependency

From the investigation of the stretch dependency we saw that increasing the normal load from 0.1 to 10 nN did not make a considerable impact on the friction in comparison to the effect associated with stretch. One special feature of our system is that we only apply load to the pull blocks, and thus one might suspect this to be of importance. Therefore, we investigate the friction under varying load for a non-cut sheet comparing the case of loading the pull block against a more traditional uniform loading of the sheet as shown in Fig. 2.14. Both load distribution shows a seemingly non-dependent relationship considering the size of our estimated error. Nevertheless, we do not see any indications that the uniform loading changes the qualitative behaviour.

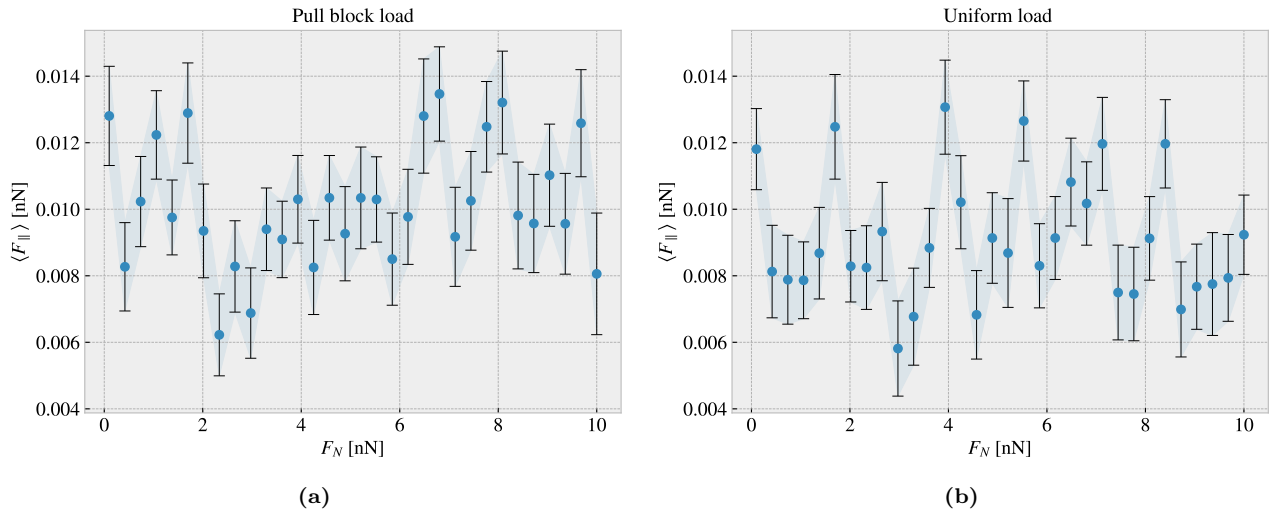


Figure 2.14: Multiple simulations of non-cut sheet under different load. Mean friction is plotted against load for two different variations of loading distribution. (a) Normal loading is applied to the pull blocks. (b) Normal loading is applied uniformly to the sheet.

In order to investigate the friction dependency of normal load for the kirigami patterns as they are stretched, we select a subset of stretch stages from Fig. 2.13b and perform additionally simulations with a logarithmically increasing normal load in the extended range 0.1–100 nN, using 30 load points for each stretch. The results are shown in Fig. 2.15. Now, when spanning three orders of magnitude for load, we start to see a noticeable increase in friction. This goes for all patterns, but it is only really visible for the non-cut sheet as the friction axis is a lot more zoomed in. Due to the fact that we have plotted the normal load on an logarithmic axis any seemingly linear trends on the figure is in fact sublinear. However, as the normal load approaches 100 nN we do start to see an increase that is more reminiscent of a linear relationship, but this is difficult to judge given that the change in friction is small in comparison to the noise in the data. Note that we omitted the error bars for visual purposes but they are one the same order of magnitude as shown in Fig. 2.14.

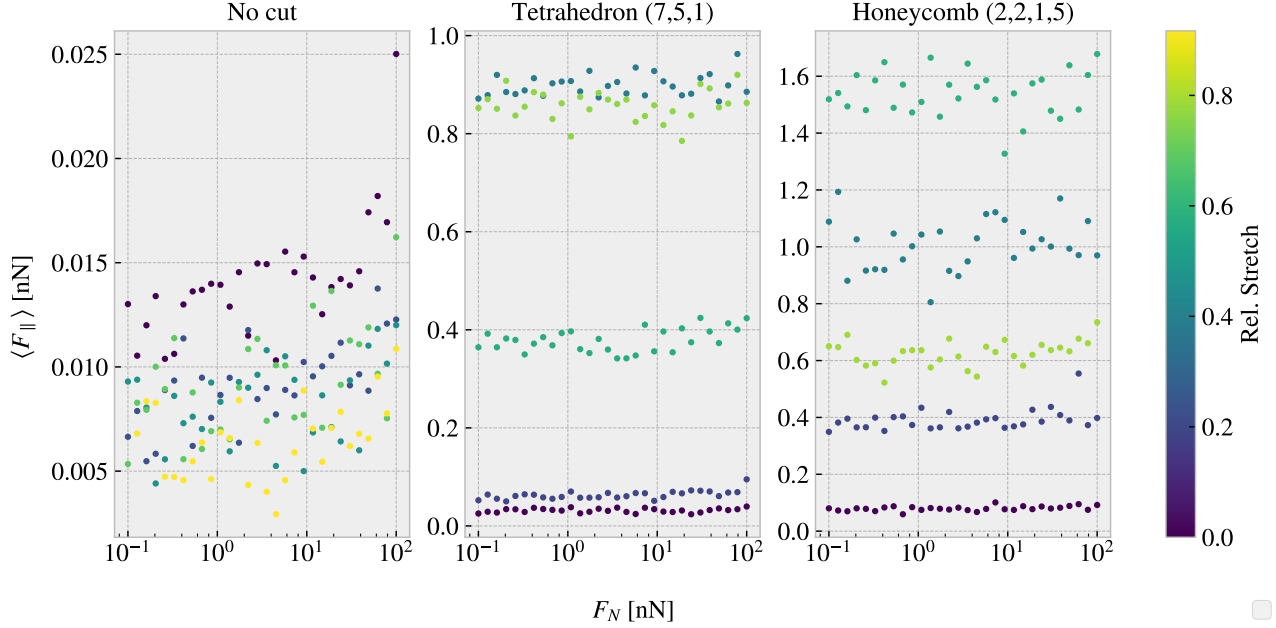


Figure 2.15: Mean friction force vs. load in the range 0.1–100 nN, for the non-cut, Tetrahedron (7, 5, 1) and Honeycomb (2, 2, 1, 5) sheet respectively, at different stretch stages relative to their rupture point.

From the friction measurements in Fig. 2.15 we see that the non-cut sheet generally produce a friction force in the order of 0.005–0.0025 nN throughout the 0.1–100 nN load range. Using a ratio based friction coefficient definition ??, $\mu_1 = F_{\text{fric}}/F_N$, this would lead to a coefficient roughly in the range

$$\mu_1, \text{ ??}: \quad \text{No cut} \sim [10^{-4}, 0.13], \quad \text{Tetrahedron} \sim [4 \times 10^{-4}, 8.7], \quad \text{Honeycomb} \sim [9 \times 10^{-4}, 15.2].$$

However, these values mainly reflect the poorness of this definition, as we find the values to diverge at low load and decrease towards high load due to the lacking linear relationship and an offset in the load curve corresponding to a finite friction at zero load. This offset is drastically enhanced for the kirigami patterns under applied stretch. Due to the small changes in friction compared to the noise in the data, it is not sensible to calculate the slope dF_{fric}/dF_N as a function of load. Nonetheless, if we force a linear fit for the whole range and use the second definition ?? as $\langle \mu_2 \rangle = \Delta F_{\text{fric}}/\Delta F_N$, we get average coefficients in the range

$$\mu_2, \text{ ??}: \quad \text{No cut} \sim [4, 9] \times 10^{-5}, \quad \text{Tetrahedron} \sim 5 \times [10^{-5}, 10^{-4}], \quad \text{Honeycomb} \sim [1, 9] \times 10^{-4},$$

depending on the stretch values. These numbers should be interpreted cautiously, but we can interpret as a rough estimate of the friction coefficient being on the order 10^{-4} – 10^{-5} . This relates to the finding by [22] who reported a seemingly non-dependent relationship between friction and normal load with increases that correspond to friction coefficients in the range 10^{-3} – 10^{-4} when using the slope definition ?. This support the idea that the graphene sheet does in fact exhibit superlubric behaviour in these conditions. Moreover, the fact that the increase with load is relatively unaffected by the stretching points to the fact that stretch induced effect mainly shift the load curve towards higher friction but do not significantly alter the slope of it. Considering the big difference in the ratio for the demonstrated friction changes with stretch (for the kirigami patterns) and the friction coefficients, we can conclude that the stretch induced mechanism is dominating the friction response. Thus, for a system where the load is coupled to a stretching mechanism, we can basically ignore any effects of loading the system and focus entirely on the stretching. Does this last sentence make sense?

Appendices

Appendix A

Appendix B

Appendix C

Bibliography

- ¹E. Gnecco and E. Meyer, *Elements of friction theory and nanotribology* (Cambridge University Press, 2015).
- ²Bhusnan, “Introduction”, in *Introduction to tribology* (John Wiley & Sons, Ltd, 2013) Chap. 1, 1–?
- ³H.-J. Kim and D.-E. Kim, “Nano-scale friction: a review”, *International Journal of Precision Engineering and Manufacturing* **10**, 141–151 (2009).
- ⁴K. Holmberg and A. Erdemir, “Influence of tribology on global energy consumption, costs and emissions”, *Friction* **5**, 263–284 (2017).
- ⁵B. Bhushan, “Gecko feet: natural hairy attachment systems for smart adhesion – mechanism, modeling and development of bio-inspired materials”, in *Nanotribology and nanomechanics: an introduction* (Springer Berlin Heidelberg, Berlin, Heidelberg, 2008), pp. 1073–1134.
- ⁶P. Z. Hanakata, E. D. Cubuk, D. K. Campbell, and H. S. Park, “Accelerated search and design of stretchable graphene kirigami using machine learning”, *Phys. Rev. Lett.* **121**, 255304 (2018).
- ⁷P. Z. Hanakata, E. D. Cubuk, D. K. Campbell, and H. S. Park, “Forward and inverse design of kirigami via supervised autoencoder”, *Phys. Rev. Res.* **2**, 042006 (2020).
- ⁸L.-K. Wan, Y.-X. Xue, J.-W. Jiang, and H. S. Park, “Machine learning accelerated search of the strongest graphene/h-bn interface with designed fracture properties”, *Journal of Applied Physics* **133**, 024302 (2023).
- ⁹Y. Mao, Q. He, and X. Zhao, “Designing complex architected materials with generative adversarial networks”, *Science Advances* **6**, eaaz4169 (2020).
- ¹⁰Z. Yang, C.-H. Yu, and M. J. Buehler, “Deep learning model to predict complex stress and strain fields in hierarchical composites”, *Science Advances* **7**, eabd7416 (2021).
- ¹¹A. E. Forte, P. Z. Hanakata, L. Jin, E. Zari, A. Zareei, M. C. Fernandes, L. Sumner, J. Alvarez, and K. Bertoldi, “Inverse design of inflatable soft membranes through machine learning”, *Advanced Functional Materials* **32**, 2111610 (2022).
- ¹²S. Chen, J. Chen, X. Zhang, Z.-Y. Li, and J. Li, “Kirigami/origami: unfolding the new regime of advanced 3D microfabrication/nanofabrication with “folding””, *Light: Science & Applications* **9**, 75 (2020).
- ¹³Z. Deng, A. Smolyanitsky, Q. Li, X.-Q. Feng, and R. J. Cannara, “Adhesion-dependent negative friction coefficient on chemically modified graphite at the nanoscale”, *Nature Materials* **11**, 1032–1037 (2012).
- ¹⁴R. W. Liefferink, B. Weber, C. Coulais, and D. Bonn, “Geometric control of sliding friction”, *Extreme Mechanics Letters* **49**, 101475 (2021).
- ¹⁵P. Zhu and R. Li, “Study of nanoscale friction behaviors of graphene on gold substrates using molecular dynamics”, *Nanoscale Research Letters* **13**, 34 (2018).
- ¹⁶S. Li, Q. Li, R. W. Carpick, P. Gumbsch, X. Z. Liu, X. Ding, J. Sun, and J. Li, “The evolving quality of frictional contact with graphene”, *Nature* **539**, Number: 7630, 541–545 (2016).
- ¹⁷J. Zhang, E. Osloub, F. Siddiqui, W. Zhang, T. Ragab, and C. Basaran, “Anisotropy of graphene nanoflake diamond interface frictional properties”, *Materials* **12**, 10.3390/ma12091425 (2019).
- ¹⁸H. Tomaç, Z. Guchan, and N. Altun, “How the stiletto heeled shoes which are popularly preferred by many women affect balance and functional skills?”, *Health Care for Women International* **43**, 1–11 (2020).
- ¹⁹K. Gibbs, *Pressure*, (2020) https://www.schoolphysics.co.uk/age16-19/Mechanics/Statics/text/Pressure_/index.html.

- ²⁰F. B. Ltd, *Foot facts*, (2023) <https://www.footbionics.com/Patients/Foot+Facts.html>.
- ²¹S. Zhang, Y. Hou, S. Li, L. Liu, Z. Zhang, X.-Q. Feng, and Q. Li, “Tuning friction to a superlubric state via in-plane straining”, *Proceedings of the National Academy of Sciences* **116**, Publisher: Proceedings of the National Academy of Sciences, 24452–24456 (2019).
- ²²M. Dienwiebel, N. Pradeep, G. S. Verhoeven, H. W. Zandbergen, and J. W. Frenken, “Model experiments of superlubricity of graphite”, *Surface Science* **576**, 197–211 (2005).